# Final Technical Report

Submitted by

Deyang Qu

| | |
|---|---|
| **Submitted To:** | U.S. Department of Energy<br>Energy Efficiency & Renewable Energy<br>Vehicle Technology Office |
| **FOA Name & Number:** | Fiscal Year 2019 Vehicle Technologies Program Wide Funding Opportunity Announcement DE-FOA-0002014 |
| **Award Number:** | DE-EE0008859 |
| **Nature of Report:** | Final Technical Report |
| **Project Period:** | October 1 2019 – September 30, 2022 |
| **Period Covered by Report:** | October 1, 2019 – September 30, 2022 |
| **Award Type:** | Cooperative Agreement |
| **Prime Recipient:** | University of Wisconsin Milwaukee |
| **Prime Recipient Type:** | Higher Education |
| **Project Title:** | Developing an In-situ Formed Dynamic Protection Layer to Mitigate Lithium Interface Shifting: Preventing Dendrite Formation on Metallic Lithium Surface to Facilitate Long Cycle Life of Lithium Solid-State Batteries |
| **Principal Investigator:** | Deyang Qu |
| **Prime Recipient DUNS Number:** | 627906399 |
| **Date of Report:** | December 30 , 2022 |
| **Signature of Submitting Official:** | 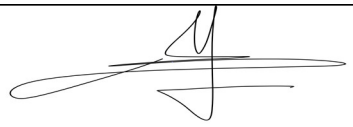 |

**Executive Summaries:**

After extensive research on various system, a fully lithiated Si anode material ($Li_{3.75}Si$) was synthesized. The high energy density, long cycle life anode demonstrated no apparent dendrite growth in an all-solid-state Li battery.

A flexible solid-state electrolyte film with a thickness less than 50 μm was developed.

All- solid-state Li full batteries were built and tested with NMC811, organic, organosulfide and sulfur cathode. Energy density of 1140 Wh/Kg at material level and 376 Wh/Kg at electrode level were demonstrated for over 500 cycles and with no apparent dendrite formation on the Li anode.

**Summarizations of project activities:**

We followed the research and development plan in the proposal based on original hypotheses. The hypotheses are that a dynamic protective layer on a Li anode needs to be established to prevent dendrite growth while a good physical contact between Li anode and SSE must be maintained. During the project period, we investigated the following three areas.

- **Li surface protection to prevent dendrite growth.**
    1. Inorganic surface lamination – carbon (graphene), red phosphorus, surface fluorination – work well in liquid electrolyte, not so well in SSE (high stacking pressure is needed).
    2. Organic additives.
    3. Alloying – **indium alloy (LiIn), fully lithiated Si-Li alloy ($Li_{3.75}Si$) – used in current studies.**
    4. Self-forming organic layer – with great potential, still working on it.
- **Cathode selection.**
    1. High Potential NMC811.
    2. Low potential organic cathode.
    3. Sulfur cathode including small molecular organosulfur cathode.
- **SSE cell diagnosis and engineering.**
    1. Lab cell, in-situ displacement and optical cells.
    2. Flexible SSE fabrication.
    3. Pouch cell and bi-polar cell development.

**Section I. Accomplishments & Milestone Update:**

**a. Major Goals of the Project**

The objective of this project is to research, develop, and test Li-metal-based batteries that implement solid LICs equipped with a formed dynamic protection layer. The proposed project aims to enable safe, long-cycle lithium anodes to achieve cell performance targets of 400 Wh/Kg, over 100 cycles, with 15 year shelf life, and < $100/KWh cost.

**b. Accomplishments**

The project was successfully completed on time and on budget. All the milestones were also accomplished.

- Long cycle life Li anode was achieved in solid state electrolytes with dynamic surface protections.

- Long cycle life full cells with metallic Li, adequate cathode and solid state electrolyte were achieved.
- Li-S full cell in coin and pouch format.
- *In-site* diagnostic tools are validated for real time observation of metal Li anode surface during operation.

**c. <u>Opportunities for Training and Professional Development</u>**

One post doctorial researcher and one Ph.D graduate student were trained in the project.

- **<u>Dissemination of results</u>**

**1, Li surface protection to prevent dendrite growth.**

We explored to build surface protective layer with inorganic and organic additives, alloying and self-forming organic layer. We down selected LiIn alloy and fully prelithiated $Li_{4.4}Si$ to be the anode for full cell builds, while the self-forming layer has great potential but needs further work.

*Dendrite growth prevention with a surface lamination.* By mean of the *in-situ* optical electrochemical cell, new Li surface coatings were tested. The surface modification aims for a dynamic dendrite growth suppression. Figure 1 shows an example of such modifications. In this particular example, dendritic Li reacted with the face layer forming a Li alloy, due to a small potential differential between the metal Li and the coating material. The Li in the alloy can be oxidized during a discharge at the similar potential to

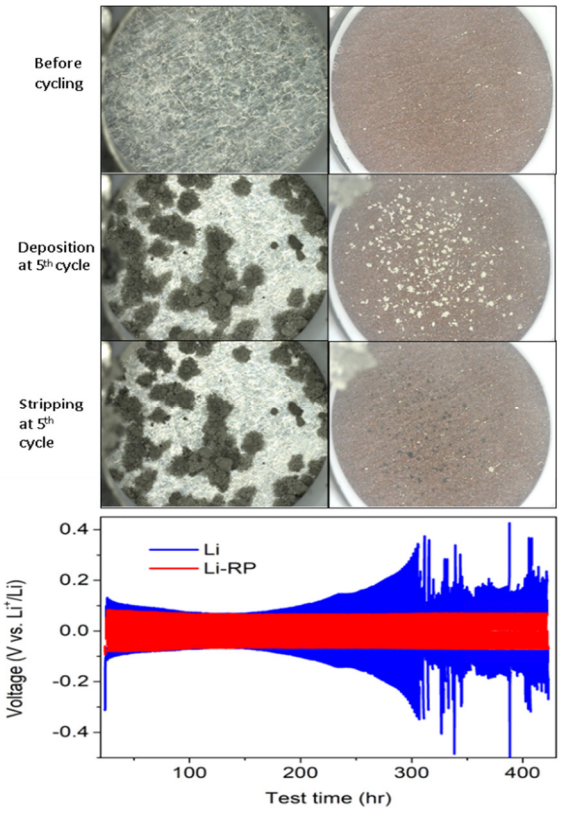


Figure 1, *in-situ* observatins of a pristine Li andoe and a surface treated Li anode after 5 cycles and the comparision of the cycle performance of a pristine Li and a surface treated Li symmetric (Li/Li) cells.

that of a metallic Li. In comparison with a pristine Li anode, no Li dendrite can be seen after five cycles. The modified Li demonstrated much longer cycle life than that of a pristine anode in a symmetric cell.

*Dendrite growth prevention with a surface self-assembled interfacial layer.* Unlike the previous one, the dynamic interfacial layer was elastic, liquid electrolyte can be trapped in the layer through a strong bonding. The size of the layer can self-adjust to compensate the volume change of the Li anode during cycling to maintain a stable electrochemical interface. Figure 2 shows the comparison of a pristine Li and a surface modified Li created by the method. The electrodes were cycled at 2 mA $cm^{-2}$ rate. The surface morphologies of the pristine and the modified anode surface are shown in the figures. Clearly, the dendrite growth and the "dead lithium formation" during cycling were substantially depressed on the modified Li surface. The artificial layer was not only formed *ex-situ*, but also can chemically "react" with Li dendrite *in-situ*. The artificial layer consisted of large conjugated system, which metallic Li can exchange electron with – one electron from a Li atom will be "dislocated" in the π conjugated system while $Li^+$ will become trapped in the matrix due to ion-ion interaction. It can be considered as the dissolution (not a chemical redox reaction) of Li dendrite in the interfacial layer. Therefore, regardless of the degree of an interfacial shift, as soon as a Li dendrite reaches the layer, Li dissolves in the layer. The Li trapped in the interface can eventually become oxidized during a subsequent discharge. Secondly with the artificial interface, the surface energy of Li anode can become more homogeneous, then the Li deposition would be more uniform. The preliminary results support these hypothesizes. The *ex-situ* formed artificial interface on Li anode could become an effective interface between Li anod and solid-state-electrolyte.

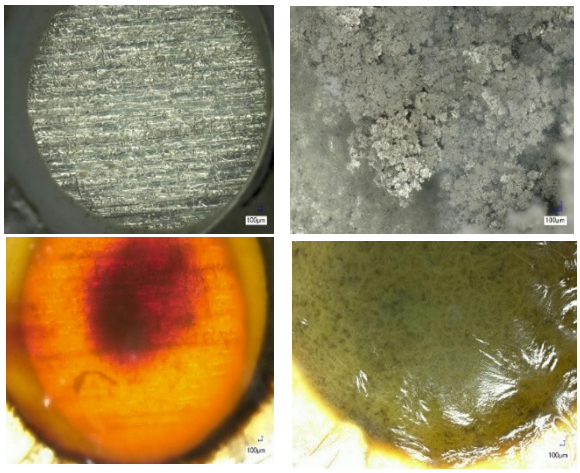

Figure 2 Pristine Li surface (up right); pristine Li after five high rate cycles (up left; elastic surface coating (down right) and after five high rate cycles (down right). The comparison of coated and pristine Li anode

*An organic cation, trisaminocyclopropenium (TAC) shown in the top of Figure 3*, was also tested to suppress dendrite growth on a metallic lithium anode. During the Li plating process, TAC cations with aliphatic chains can form a positively charged electrostatic shield around Li protrusions, repelling the approaching Li+ and thereby attaining a more uniform plating. A two times longer cycle life of 300 h at 1 mA $cm^{-2}$ is achieved in a Li‖Li symmetric cell in comparison with the control. Eventually, the TAC molecular will be polymerized by attaching to a backbone or distributed in a polymer matrix. The objective is to form a dynamic interface between the Li anode and the solid-state-electrolyte.

To investigate the role of TAC cation on dendrite suppression, the polarization profiles of Li‖Li symmetric cells were first cycled at 1 mA $cm^{-2}$ rate for 1-hour duration. As displayed in Figure II.9.M.6 (a), the cell with TAC performs significant better than the baseline. In a baseline cell, Coulombic

efficiencies (CEs) dropped below 90% after 49 cycles, while an average CE of 97% was preserved with TAC throughout 135 cycles (Figure II.9.M.6 (b)). The *in-situ* optical microscopic images were compared under a harsh Li plating condition of 4.0 mA $cm^{-2}$. As displayed in Figure II.9.M.6 (d), highly dendritic and

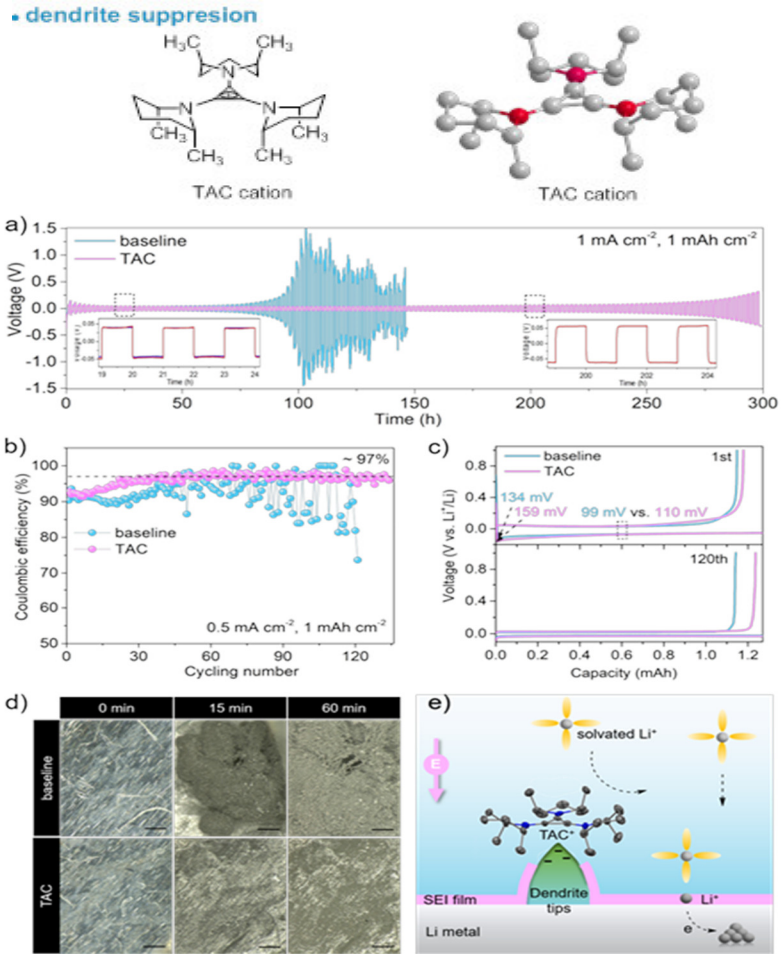


Figure 3, (Top) Molecular structure of trisaminocyclopropenium (TAC). (bottom) Electrochemical performance of Li plating/stripping in TAC electrolyte. a) Voltage profiles of Li‖Li symmetric cells cycling at 1 mA cm-2 1 mAh cm-2; b) Coulombic efficiencies of Li‖Cu asymmetric cells cycling at 0.5 mA cm-2 1 mAh cm-2 and c) the voltage profiles of Li‖Cu cell at 1st and 120th; d) in-situ optical microscopic images during Li plating process at 4 mA cm-2, scale bar 200 μm; e) schematic illustration of a cation-shield mechanism. Note: the TAC is not drawn to scale.

mossy Li formed after 15 min in the baseline electrolyte and evolved into filament morphology after 60 min. These dead Li can lead to a poor CE and an increased cell impedance. In contrast, a relatively uniform Li deposition was observed in the TAC electrolyte throughout the test.

A cation-shield mechanism is proposed and illustrated in Figure 3. It is well established that the plating process can unavoidably generate protuberant tips on which electric charges tend to accumulate. The TAC cations can be absorbed on those tips without being reduced via electrostatic attraction. Thus, a lithiophobic protective layer can be formed due to its bulky scaffold with branched nonpolar groups. The arriving $Li^+$ was repelled and deposited on the adjacent flat Li surface, thus generating a dendrite-free Li deposition.

*Fully prelithiated all-electrochem-active Si anode for the mitigation of dendrite growth.* The as-synthesized $Li_xSi$ is relatively soft, highly electronically conductive, and with a high Li diffusivity. These distinctive properties make $Li_xSi$ anode viable as an "all-electrochem-active" electrode (consisted of 100 wt.% $Li_xSi$). Compared with the typical composite electrode, the all-electrochem-active electrode not merely maximizes the electrode-level energy density but also minimizes the electrolyte-related interfacial degradation. $Li_xSi$ symmetric cell demonstrates a reversible cycling at 4 mA $cm^{-2}$ for over 320 h. Stress change and morphological evolution of the $Li_xSi$ electrode are investigated upon dealloying/alloying.

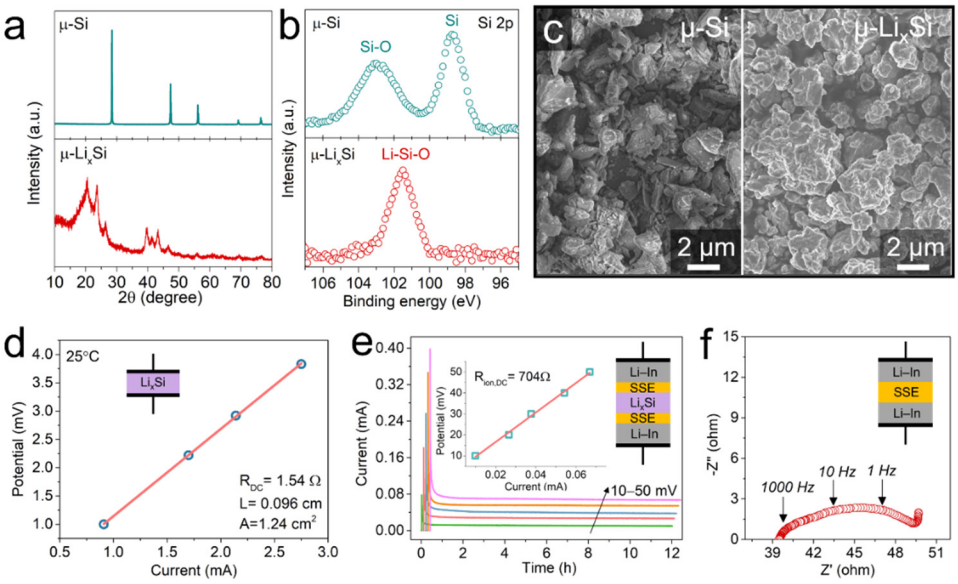


Figure 4 a) X-ray diffraction profiles. b) XPS spectra of the Si 2p region. c) SEM images of the pristine μ-Si and the as-synthesized μ-$Li_xSi$. d) Electronic conductivity measurement of μ-$Li_xSi$. e) DC polarization measurement of Li-In|SSE|μ-$Li_xSi$|SSE|Li-In symmetric cell. f) AC impedance measurement of Li-In|SSE|Li-In symmetric cell.

Figure 4 displays the X-ray diffraction (XRD) profiles. After prelithiation process, the pristine crystalline μ-Si (Fig. 4a, up) transformed to amorphous $Li_{3.75}Si$ ($Li_{15}Si_4$) phase (Fig. 4a, bottom), as indicated by the newly emerged peaks at ca. 21°, 24°, 27°, 40°, and 43.5°. Despite the Li/Si molar ratio of the precursors is 4.4/1, ca.10% extra Li is still required to obtain a phase pure $Li_{4.4}Si$ ($Li_{22}Si_5$) compound. Since some unavoidable side reactions related with the surface impurities of the pristine Si particles need to consume extra Li during milling process. The as-synthesized $Li_{3.75}Si$ compound (denoted as μ-$Li_xSi$ thereafter) was then used for the following study. X-ray photoelectron spectroscopy (XPS) analysis of the pristine μ-Si in Fig. 4b shows two peaks in the region Si 2p, representing the Si–Si bond (98.5 eV) and the Si–O bond (103 eV). The Si–O bond originated from the native oxide layer ($Si_xO_y$) existed on the surface of Si particles. After lithiation, the new peak occurring at 101.5 eV was assigned to the Li–Si–O bond formed within $Li_xSi$ matrix. Scanning electron images (SEM) show that the pristine μ-Si were separate particles with rigid edges (Fig. 4c, left), while the particles became expanded and interconnected with smoother edges after lithiation (Fig. 4c, right).

The pristine μ-Si showed an electronic conductivity of $10^{-2}$ mS $cm^{-1}$ and barely had any ion diffusivity. After lithiation, μ-$Li_xSi$ exhibited three orders of magnitude higher electronic conductivity (50.3 mS $cm^{-1}$) (Fig. 4d). To evaluate the Li conductivity of μ-$Li_xSi$, direct current (DC) polarization measurement was carried out on Li-In|SSE|μ-$Li_xSi$|SSE|Li-In cell, where the SSE layer acted as an electron-blocking electrode. As illustrated in Fig. 4e, the overall DC resistance includes two SSE layers ($2R_{ion,SSE}$), two Li-In|SSE interfaces ($2R_{Li\text{-}In|SSE}$), one μ-$Li_xSi$ layer ($R_{ion,\mu\text{-}LixSi}$), and two μ-$Li_xSi$|SSE interfaces ($2R_{\mu\text{-}LixSi|SSE}$). To estimate the resistance contributed by the SSE layer and the Li-In|SSE interface, a Li-In|SSE|Li-In cell was further fabricated; its AC impedance is shown in Fig. 4f. The resistance of SSE layers ($2R_{ion,SSE}$) and Li-In|SSE interface ($2R_{Li\text{-}In|SSE}$) was around 49.5 Ω $cm^2$. Therefore, the Li conductivity of the μ-$Li_xSi$ layer was roughly calculated to be > 0.1 mS $cm^{-1}$, since it was hard to decouple the resistance of $Li_xSi$|SSE interface from the overall resistance.

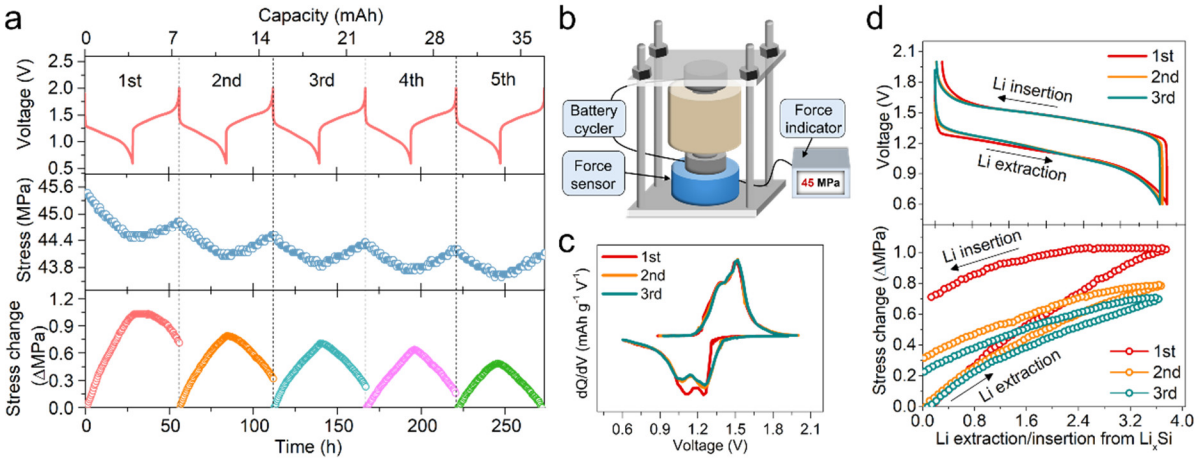


Figure 5 a) The voltage profiles of μ-$Li_xSi$|SSE|LTO cell (up) along with correlated evolution of stress (middle) and stress change (bottom). b) Schematic of pressure-monitoring cell. c) Corresponding dQ/dV curves. d) Voltage and stress change plotted as a function of the molar amount of lithium extracted from or inserted into the μ-$Li_xSi$ phase.

The volume change of μ-$Li_xSi$ electrode was explored by *in-situ* monitoring the dynamic pressure change of μ-$Li_xSi$|SSE|$Li_4Ti_5O_{12}$ full cell. Since the phase transition of $Li_4Ti_5O_{12}$ (LTO) cathode causes negligible volume change, the net stress change of the full cell is governed by the μ-$Li_xSi$ anode alone. Voltage profiles of full cell (Fig. 5a, up) along with the correlated evolution of stress (Fig. 5a, middle) and the stress change (Fig. 5a, bottom) were recorded over five consecutive cycles. Fig. 5b illustrates the stress measurement setup and Fig. 5c shows the corresponding dQ/dV curves. With an areal capacity of ≈3 mAh $cm^{-2}$, the full cell exhibited ≈0.7 MPa stress swing upon cycling, with a stress decrease during discharge (Li extracted from μ-$Li_xSi$) and an increase during charge (Li inserted to μ-$Li_xSi$). Theoretically, the stress change only depends on the quantity of Li inserted or extracted from the μ-$Li_xSi$ electrode, which is proportional to the areal capacity. But in real scenarios, the stress change can be weakened due to the elastic deformation of SSE layer and the presence of pores and void spaces within the cell. For example, the thicker the SSE layer is, the smaller stress change would be detected. As shown in Fig. 5a (bottom) and Fig. 5d (bottom), a relatively large stress hysteresis (irreversibility of stress change) is revealed from the initial cycle, which gradually vanishes in the subsequent cycles. At the $5^{th}$ cycle, the stress change became highly reversible upon charge/discharging (Fig. 5a, bottom). The weakening of stress hysteresis could be attributed to the rearrangement of pristine void space within the cell along the contraction and expansion of μ-$Li_xSi$ at the initial cycles. Also, stress hysteresis caused by the irreversible trap of some active Li inside the LTO structure during the $1^{st}$ cycle, as revealed by the initial Coulombic efficiency of 97.0% (Fig. 5d up), would disappear in the following cycles.

**2, Cathode selection.**

*High voltage ASSE Li battery with NMC811 cathode*. The most popular inorganic SEs are lithium thiophosphastes which are good ionic conductors. However, the inherent instability at high potentials limits their application in the 4V batteries. Halide-based electrolytes have attracted ever-rising interest lately. Halides exhibit combined advantages of sulfides and oxides, including easy processability and (electro)chemical stability toward high-voltage cathodes. However, the poor reduction stability of halides in contact with lithium metal remains an open challenge. To tackle the problem, Li-Y alloys (Y=In, Sn, Ge) or metallic In to replace Li metal as anode, which sacrifices the cell overall energy density by lowering the operating potential.

Based on the investigation of the reaction mechanisms, we constructed a kinetically stable interface by inserting an argyrodite buffer layer between Li metal and $Li_3YCl_6$ layer, a representative halide electrolyte. Argyrodite ($Li_6PS_5Cl$) was selected due to its fast ionic conduction, soft mechanical property, and more importantly, its ability to produce a kinetically stable interface in contact with Li metal. We demonstrate Li/Li symmetric cell with a polarization potential as low as 100 mV and a stable plating/stripping behaviour over 1000 h at 0.2 mA $cm^{-2}$, 0.2 mAh $cm^{-2}$. Moreover, $LiNi_{0.8}Co_{0.1}Mn_{0.1}O_2$/Li full solid-state cell delivers a record-breaking high initial Coulombic efficiency of > 87%. To the best of our knowledge, this is the first case to employ Li metal as anode in halide-based all-solid-state batteries.

The high oxidation stability of halide SEs allows the use of commercial 4V-class $LiMO_2$ (M=Ni, Co, Mn, Al) cathodes without any protective coating layer. To investigate full cell performance, cathode composite was made by hand grinding LYCl SE, bare $LiNi_{0.8}Co_{0.1}Mn_{0.1}O_2$ (NCM-811) powder, and conductive carbon at a weight ratio of 60:30:10. The charge/discharge voltage profiles of NCM-811/LYCl/Li full cell and NCM-811/LYCl/LPSCl/Li full cell were compared in Fig. 6 a-b. The current density is 0.1 mA $cm^{-2}$ and the loading of NMC-811 is 6 mg $cm^{-2}$. At the initial cycle, NCM-811/LYCl/Li full cell exhibited a high charging capacity of 255 mAh $g^{-1}$ and a low Coulombic efficiency (CE) of 65%. In the following cycles, the electrochemical polarization continuously increased. At the $12^{th}$ cycle, the charging curve showed a long voltage plateau at 4.05 V and failed to reach the upper cut-off voltage of 4.3 V. This could be caused by continuous reaction between freshly deposited lithium and LYCl during delithiation process. By contrast, the NMC-811/LYCl/LPSCl/Li full cell delivered a capacity of 181 mAh $g^{-1}$ and 183 mAh $g^{-1}$ for the first two cycles, with a CE of 87% and 98%, respectively (Fig. 6 b). As marked in the blue circle, no additional slope occurs prior to reaching the charge plateau, indicating no formation of space charge layer at the NCM-811/LYCl interface. A higher active material content leads to an even higher ICE of 89%. Typical curves representing the three-phase transition process of NCM-811 material can be clearly observed from dQ/dV curves (insert Fig. 6 b) and CV profiles (Fig. 6 c). The EIS evolution of full cell during one charge/discharge cycle (Fig. 6 d) validates high interfacial stability of both LYCl/NCM-811 interface and LPSCl/Li interface. The full cell displayed stable cycling with a capacity retention of 91 % and a high CE of 99.7 % after 100 cycles (Fig. 6 e). Fig. 6 f displayed the rate capability and a reversible discharge capacity of 90 mAh $g^{-1}$ was achieved at 1C rate.

*Organic Cathode.* Many organic compounds were test as cathode materials in SSE Li batteries. For example, collaborating with Millipore Aldrich, Polyimide-graphene (PI-G) nanocomposite was synthesized through an *in-situ* polycondensation process from two inexpensive stock compounds, 1,4,5,8-naphthalenetetracarboxylic dianhydride and ethylenediamine. Functionalized graphene sheets were incorporated during the process to enhance the electronic conductivity of PI. The electronic conductivity of the as-synthesised PI-G composite was measured to be 16.5 mS $cm^{-1}$ at 25 °C, which outperformed most of the common inorganic cathode materials ($10^{-6}$–$10^{-4}$ S $cm^{-1}$). PI-G was used as the cathode material in the ASSLB using a thin $Li_6PS_5Cl$ solid electrolyte.

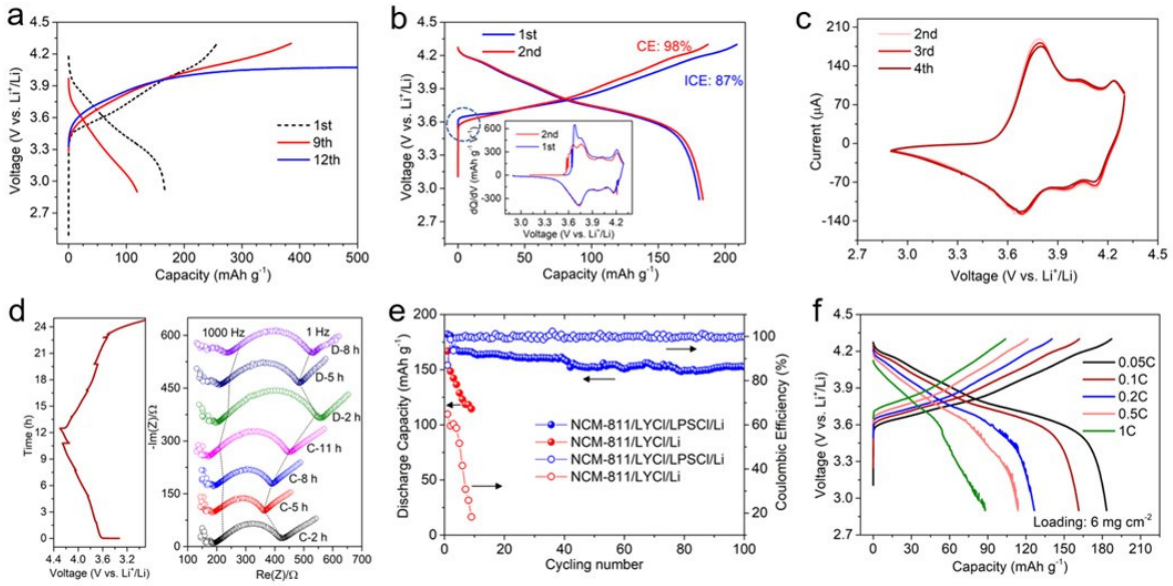


Figure 6 a) Charge/discharge profiles of NCM-811/LYCl/Li cell at 0.1 mA $cm^{-2}$. Electrochemical performance of NCM-811/LYCl/LPSCl/Li cell: b) initial two charge/discharge profiles at 0.1 mA $cm^{-2}$ (corresponding dQ/dV curves shown insert); c) CV profiles at 0.02 mV $s^{-1}$; d) impedance evolution during one charge/discharge cycle. e) cycling performance at 0.1 mA $cm^{-2}$; f) rate capability from 0.1 C to 1 C.

A PI|$Li_6PS_5Cl$|Li cell was assembled to investigate the electrochemical performance of the PI cathode. The XRD pattern in Fig. 7a verifies a well-formed cubic structure of the $Li_6PS_5Cl$ phase. The redox behaviour of PI can involve a maximum of four-electron transfers, but only two electrons can be reversibility utilized from each formula unit above 1.5 V (vs. $Li^+$/Li), corresponding to a theoretical capacity of 183 mAh $g^{-1}$. Fig. 7b (up) illustrates the formation of a radical dianion within a carbonyl unit after 2-electron reduction. CV profiles shown in Fig. 7b (down) display a pair of broad redox peaks at ~2.2 V (vs. $Li^+$/Li). Galvanostatic voltage profiles at following cycles in Fig. 7c display an attainable capacity of ~190 mAh $g^{-1}$ at 60 °C within the voltage range of 1.4–3.6 V (vs. $Li^+$/Li). The inset dQ/dV curves corresponded well with the CV results and displayed a high consistency over cycling. The decomposition products of $Li_6PS_5Cl$ may contribute to the overall cell capacity, which explained why the attainable capacity exceeded the theoretical value of PI. Fig. 7d demonstrates a stable cycling performance of the PI cathode over 100 cycles at 0.1 C (the slight capacity increase could be a result of temperature fluctuation). Rate performance in Fig. 7e-f shows that the capacity of PI cathode remains at 80 mAh $g^{-1}$ at 0.7 C, corresponding to 42% of its initial capacity.

Galvanostatic intermittent titration technique (GITT) was further employed to study the polarization of the electrochemical reaction. A series of current pulses (0.05 C) were applied to the system, with each followed by a 4 h relaxation. During the relaxation, the cell tended to become homogenous by $Li^+$ diffusion and approach an equilibrium. The PI cathode in Fig. 7g presents only one voltage plateau after full relaxation, indicating a one-step solid-solid phase transition between $Li_x$-PI and PI. Polarization curves can reflect the evolution of interfacial resistance through monitoring the iR drop under different potentials. A build-up of polarization was observed in Fig. 7h when the system was discharged below 2 V or charged above 2.5 V. The increase of ohmic resistance is attributed to the hindrance of ionic diffusion inside $Li_6PS_5Cl$ electrolyte due to oxidative/reductive decomposition. It should be noted that the $Li_6PS_5Cl$ had a narrow electrochemical stability window (1.7–2.0 V vs. $Li^+$/Li). Also, the variation of ionic conductivity could establish a $Li^+$ concentration gradient perpendicular to the cathode surface, which

would be more pronounced in a thick electrode design. Despite causing the overall impedance increase, these decomposition products were mostly redox-active and would render a reversible evolution of the interfacial layer. Fig. 7i shows a crack-free cathode layer and SSE layer after cycling. Fig. 7j shows no obvious dendrite formation at the SSE|Li interface and the thickness of Li anode decreased by 13% (from 45 μm to 39 μm), possibly due to consumption by reacting with SSE to form a kinetically stable anode interface.

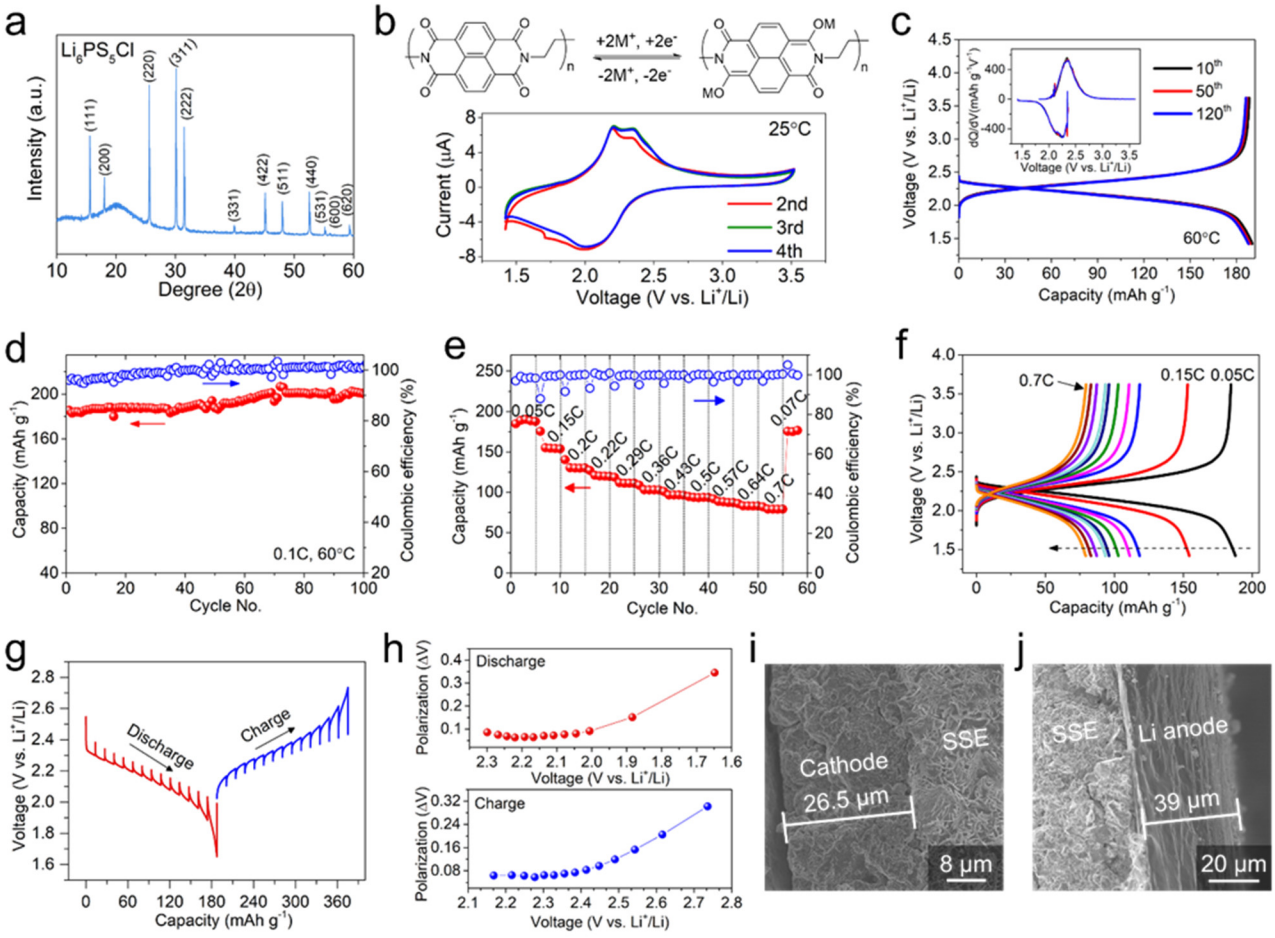


Figure 7. a) XRD pattern of $Li_6PS_5Cl$ electrolyte. b) Schematic of redox process of PI ($M^+$ stands for $Li^+$ and $Na^+$) and its CV profiles at a scan rate of 0.02 mV $s^{-1}$. c) Galvanostatic voltage profiles of pellet-type PI|$Li_6PS_5Cl$|Li cell and inset is the corresponding dQ/dV curves. d) Cycling performance at 0.1C (1C =180 mA $g^{-1}$). e) Rate performance and f) voltage profiles from 0.05 C to 0.7 C. g) GITT potential profile and h) polarization plots throughout one discharge/recharge cycle. Cross-sectional SEM images of i) cathode|SSE interface and j) SSE|Li interface after cycling.

*Sulfur cathode.* As shown in figure 8, full cell performance was evaluated by pairing a S cathode with a pure Li anode, a Li-In alloy anode, and a μ-$Li_xSi$ alloy anode, respectively. $Li_xSi$|SSE|S cell displayed a discharge voltage plateau of 1.75 V, which is 280 mV higher than that compared with Li-In|SSE|S cell. The discharge plateau represents the solid–solid conversion between S and $Li_2S$ occurred within the S cathode. Long-term cycling tests were next carried out. Li-In|SSE|S cell showed a rapid capacity fading after 50 cycles and became shorted at the 88$^{th}$ cycle. It is noteworthy that a relatively high mass loading and high current condition could cause cavity formation at the Li-In|SSE interface and unexpectedly Li-In

filament growth, which would result in capacity decay and cell failure. In comparison, μ-$Li_xSi$|SSE|S cell in showed stable cycling and retained 85.4% capacity after 200 cycles. Under high current rates, LiIn cell only delivered 427 mAh $g^{-1}$ under 1C while $Li_xSi$ cell can still deliver 1301 mAh $g^{-1}$, implying the much faster alloying reaction of $Li_xSi$.

Room-temperature operation has been a long-standing challenge to achieve ideal practical application of ASSBs. Therefore, cycle life and rate capability of μ-$Li_xSi$|SSE|S cell were evaluated at 25°C. Fig. 8 shows 76.3% capacity was retained after 300 cycles under 0.3C. Under 1.2C, an accessible capacity of 866 mAh $g^{-1}$ was achieved, corresponding to 69% of the capacity under 0.05C (1249 mAh $g^{-1}$).

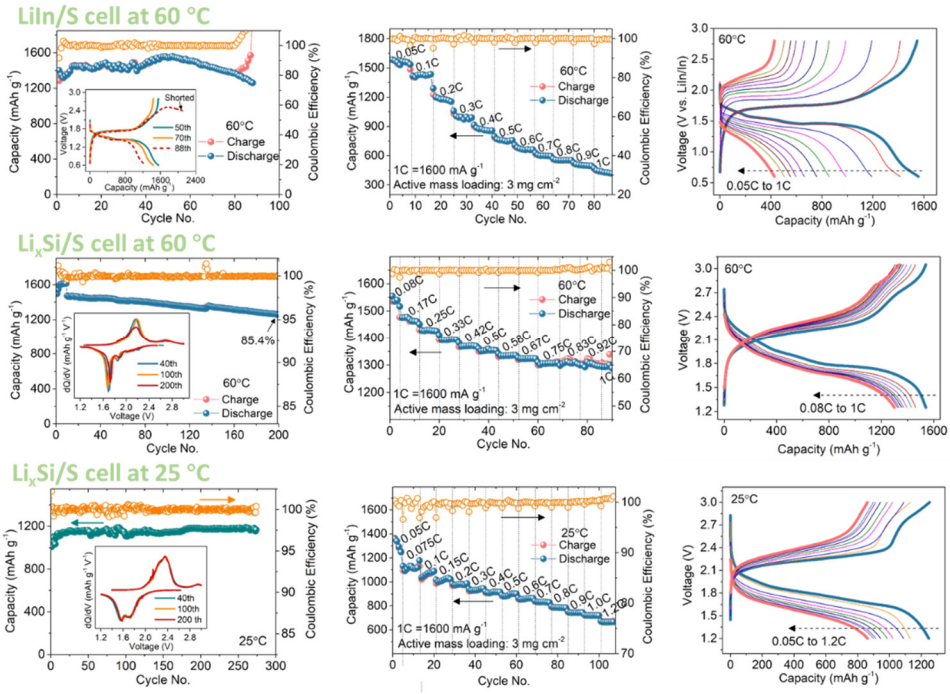


Figure 8 Cycling, rate performance of Li-In|SSE|S full cell at 60°C (1st row); μ-$Li_xSi$|SSE|S full cell at 60°C (2nd row); μ-$Li_xSi$|SSE|S full cell at 25°C (3rd row).

### 3. A flexible, highly conductive thin SSE and the fabrication of a Li-S pouch cell

Despite the successful efforts on boosting the material- and electrode-level energy density, strategies to increase the cell-level energy density have rarely been reported. Most of the reported cells were based on a pellet-type configuration manufactured by dry powder die compression. The obtained SSE separator was rather thick (0.5–1.0 mm) and the cathode areal loading was relatively low (< 2mg $cm^{-2}$), resulting in an extremely low cell-level energy density (<50 Wh $kg^{-1}$) and a high cell internal resistance. The major challenge for reducing the separator thickness is the brittleness of ceramic materials, a problem which is exacerbated under a practical condition, as the area to thickness ratio of the separator increases. Therefore, developing feasible technology to manufacture thin but robust SSE is an imperative need for exploiting commercialization-driven ASSBs.

We fabricated a remarkable free-standing SSE membrane, which was merely 46 μm thick, and an ultralow areal resistance of 3.3 Ω $cm^2$ was achieved, more than tenfold lower than that of reported SSE pellets.

A thick SSE can not only reduce the cell-level energy density but also cause an exceptionally high areal resistance, based on the equation $R = {}^{l}/_{\sigma}$, where $R$ ($\Omega$ cm$^2$) is the areal resistance, $l$ (cm) is the thickness, and $\sigma$ (S cm$^{-1}$) is the conductivity, respectively. Such a high areal resistance would inevitably result in a high cell resistance and poor power performance, undermining the intrinsic benefits of high conductivity of sulfide superionic conductors. Therefore, developing a thin (<50 μm) but robust SSE membrane should take precedence over other factors in commercializing sulfide-based Li-organic batteries. In this study, the dry process was used to manufacture $Li_6PS_5Cl$ membrane. Despite the binder content being merely 0.2 wt.%, the as-fabricated SSE membrane in Fig. 9a was free-standing and demonstrated a high flexibility. After cold pressing, the SSE thickness was reduced from 70 μm (Fig. 9c) to 46 μm (Fig. 0c), with a compaction density of 2.6 g cm$^{-3}$. As marked by the arrows, the PTFE fibrils were well retained within the much-densified SSE structure. The ionic conductivity of SSE membrane was measured to be 1.4 mS cm$^{-1}$ (Fig. 9d), which was slightly lower than that of the binder-free SSE pellet (1.8 mS cm$^{-1}$), owing to the ionic insulating nature of PTFE. Despite this fact, the areal resistance was a mere 3.3 $\Omega$ cm$^2$, more than tenfold lower than the SSE pellet (39 $\Omega$ cm$^2$, we used 0.7 mm thickness in the calculation).

It is worth mentioning that PTFE would decompose once in contact with lithium to generate defluorinated carbon, which is electronically conductive. The propagation of the reaction will eventually cause the short of the membrane. We are in the process of overcoming the obstacle, but in the meantime, $Li_{38}In_{62}$ alloy (0.62 V vs. $Li^+/Li$) was used as an anode. In order to test the flexible SSE membrane, a polyimide was used as the cathode in a sheet-type polyimide|$Li_6PS_5Cl$|LiIn full cell. Polyimide is a durable and low-cost engineering plastic with high thermal resistance, chemical inertness, and insolubility in common organic solvents. It was also proven to be a high-performance cathode material in lithium-ion batteries and tested in many stationary energy storage systems. We chose the material to be a cathode test vehicle. The polyimide|$Li_6PS_5Cl$|LiIn full cell in Fig. 9e shows a discharge plateau of 2.2 V (vs. $Li^+/Li$) and an attainable capacity of ~180 mAh g$^{-1}$, which is consistent with that of the pellet-type cells. Cycling performance in Fig. 9f shows almost no capacity decay with an average Coulombic efficiency >99% over 30 cycles. To the best of our knowledge, this is the first demonstration of a sulfide-based organic ASSB with a sheet-type cell design. Energy densities were compared among these works based on considering only the cathode and the SSE part, since the anode can be further optimized. The calculated volumetric energy density was 164.2 Wh L$^{-1}$ and the gravimetric energy density was 100.3 Wh kg$^{-1}$. The energy density was more than tenfold higher than the value of other works despite the mediocre intrinsic capacity of polyimide. It should be noted that PI was only employed as a test vehicle here, but the dry-film technique can be extended to many other thermally stable and sulfide SSE-compatible cathodes.

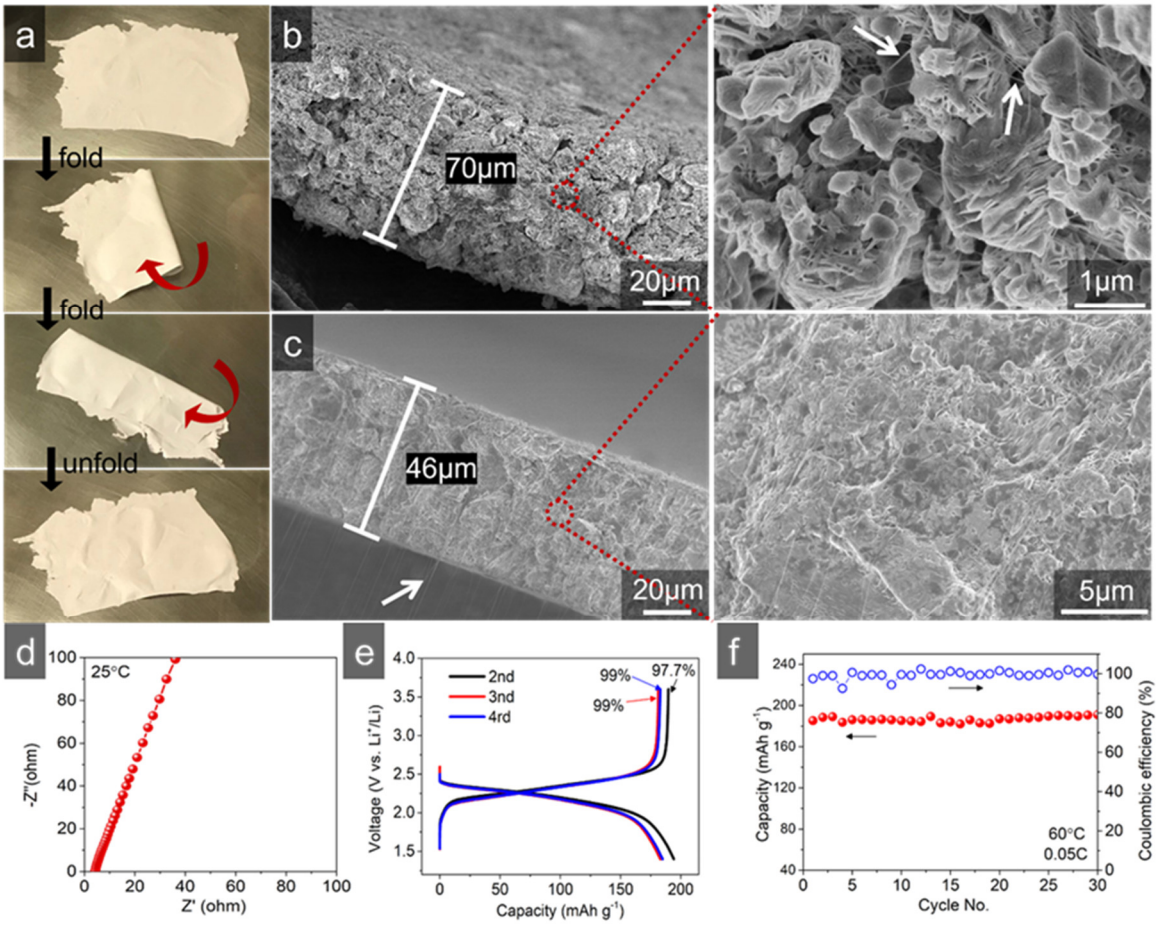


Figure 9 a) Flexibility test of the free-standing SSE membrane. b) Cross-sectional SEM images of SSE membrane b) before and c) after cold pressing. d) Ionic conductivity measurement of SSE membrane at 25 °C. e) Galvanostatic voltage profiles and f) cycling performance of sheet-type Polyimide|$Li_6PS_5Cl$|LiIn cell at 60 °C.

The ultimate goal of the flexible SSE is to fabricate a large format pouch cell. After verifying the electrochemical performance of the PTFE bond flexible SSE, a sulfur|$Li_6PS_5Cl$|LiIn full cell in a pouch cell format was built. Figure 10 shows the 2x3 inch pouch cell, the test fixture and the first a few cycles of the cell. The initial capacity of the cell was above 1100 mAh/g (of sulfur). As shown in the figure, although the ASSE Li-S cell can light a LED without external pressure, about 500 KPa was still appled to discharge the cell.

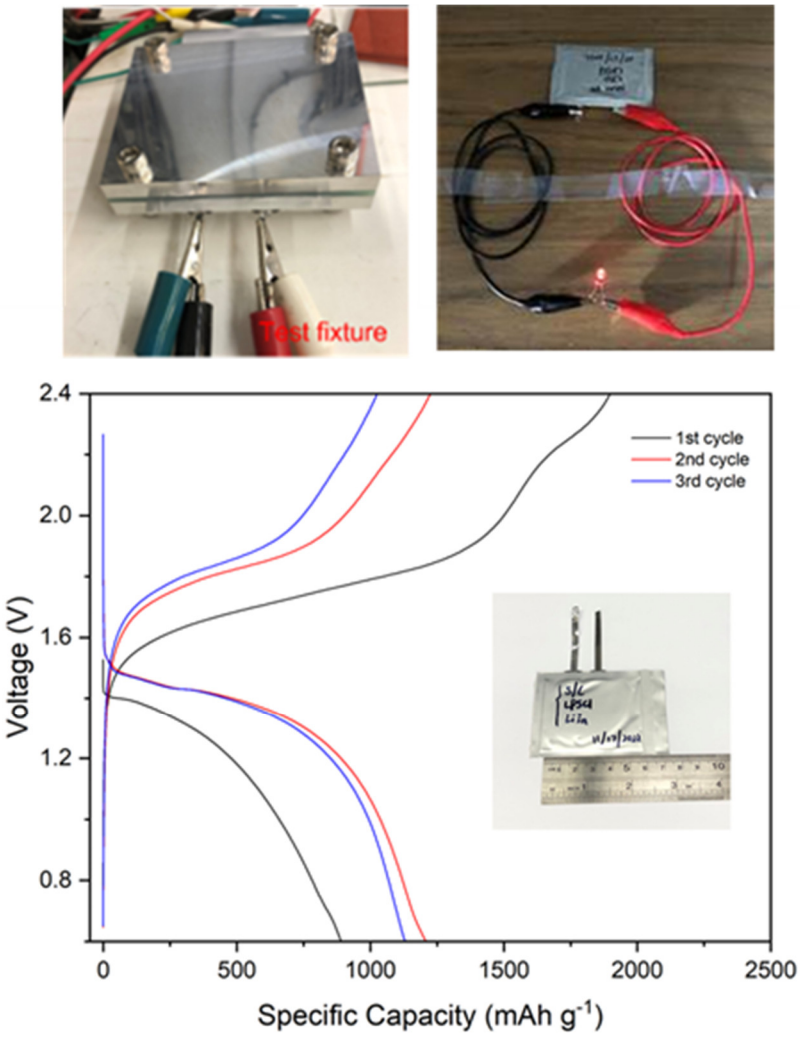


Figure 10 All solid-state state sulfur|Li6PS5Cl|LiIn cell pouch cell (full cell, 2x3 inch), cell under test in a pressure fixture and first 3 cycles @60oC.

## Section II. Products/Project Output:

### a. Publications:

#### i. Accepted Manuscripts of Journal Articles

1. Weixiao Ji,, He Huang,, Dong Zheng, Xiaoxiao Zhang, Tianyao Ding, Tristan H. Lambert, Deyang Qu, "A Redox-Active Organic Cation for Safer Metallic Lithium-Based Batteries", Energy Storage Material 32(2020)185-190.

2. Weixiao Ji, Dong Zheng, Xiaoxiao Zhang, Tianyao Ding, Deyang Qu, "Kinetically Stable Anode Interface for Li3YCl6-based All-Solid-State Lithium Batteries" J. Mat. Chem. A 9(2021)15012-15018.

3. Weixiao Ji, Xiaoxiao Zhang, Le Xin, Avery Luedtke, Dong Zheng, He Huang, Tristan Lambert, Deyang Qu*, “A high-performance organic cathode customized for sulfide-based all-solid-state batteries”, Energy Storage Material, 45(2022)680

4. Weixiao Ji , Xiaoxiao Zhang , Huainan Qu, Le Xin, Avery T. Luedtke, He Huang, Tristan H. Lambert, Deyang Qu*, “Polyimide as a durable cathode for all-solid-state Li(Na)−organic batteries with boosted cell-level energy density”, Nano Energy 96 (2022)107130.

5. Weixiao Ji, Xiaoxiao Zhang, Dong Zhang, He Huang, Tristan Lambert, Deyang Qu*, “Practically Accessible All-Solid-State Batteries Enabled by Organosulfide Cathodes and Sulfide Electrolyte”, Adv. Funct. Mater. 2022 2202919.

6. Weixiao Ji, Xiaoxiao Zhang, Miao Liu, Tianyao Ding, Huainan Qu, Dantong Qiu, Dong Zheng, Deyang Qu*, “High-performance all-solid-state Li–S batteries enabled by an all-electrochem-active prelithiated Si anode”, Energy Storage Material,53(2022)613-620

**ii. <u>Other publications, conference papers and presentations</u>**

“An All-Solid-State Li-Oranosulfide Battery with an Ultrathin Flexible Solid-State Electrolyte”, ACS Fall Meeting Sulfide-Based Solid-State Electrolytes & Batteries, 08/21/2022, Chicago